In vivo base editing rescues hearing in humanized *MPZL2* mice within a structure-dependent therapeutic window

Sohyang Jeong[1#], Byeong-Hee Kang[1#], Won Hoon Choi[1#], Yeji Choi[1#], Hansol Koo[2#], Woo Seok Byun[1], Yejin Yun[1], Sung Ho Jung[1], Juhye Choi[1], Chanju Jung[3], Dong Woo Nam[1], Heeyoung Seok[4], Seunghee Cho[5], Sung-Yeon Lee[6,7], Sangsu Bae[2,3,8]*, Sang-Yeon Lee[1,9]*

[1]Department of Otorhinolaryngology-Head and Neck Surgery, Seoul National University Hospital, Seoul National University College of Medicine, Seoul, Republic of Korea.

[2]Cancer Research Institute, Seoul National University College of Medicine, Seoul 03080, Republic of Korea.

[3]Department of Biomedical Sciences, Seoul National University College of Medicine, Seoul 03080, South Korea

[4]Department of Transdisciplinary Research and Collaboration, Genomics Core Facility, Biomedical Research Institute, Seoul National University Hospital, Seoul, Republic of Korea

[5]AAVATAR Therapeutics, 12925, Gyeonggi-do, Republic of Korea.

[6]GEM Division, Macrogen Inc., Seoul, South Korea, 07573.

[7]Laboratory of Theriogenology, College of Veterinary Medicine, Seoul National University, Seoul, South Korea, 08826.

[8]Genomic Medicine Institute, Seoul National University College of Medicine, Seoul 03080, Republic of Korea.

[9]Sensory Organ Research Institute, Seoul National University Medical Research Center, Seoul, Republic of Korea.

[#]These authors contributed equally.

*To whom correspondence should be addressed to S-Y.L. (maru4843@hanmail.net) and S.B. (sbae7@snu.ac.kr)

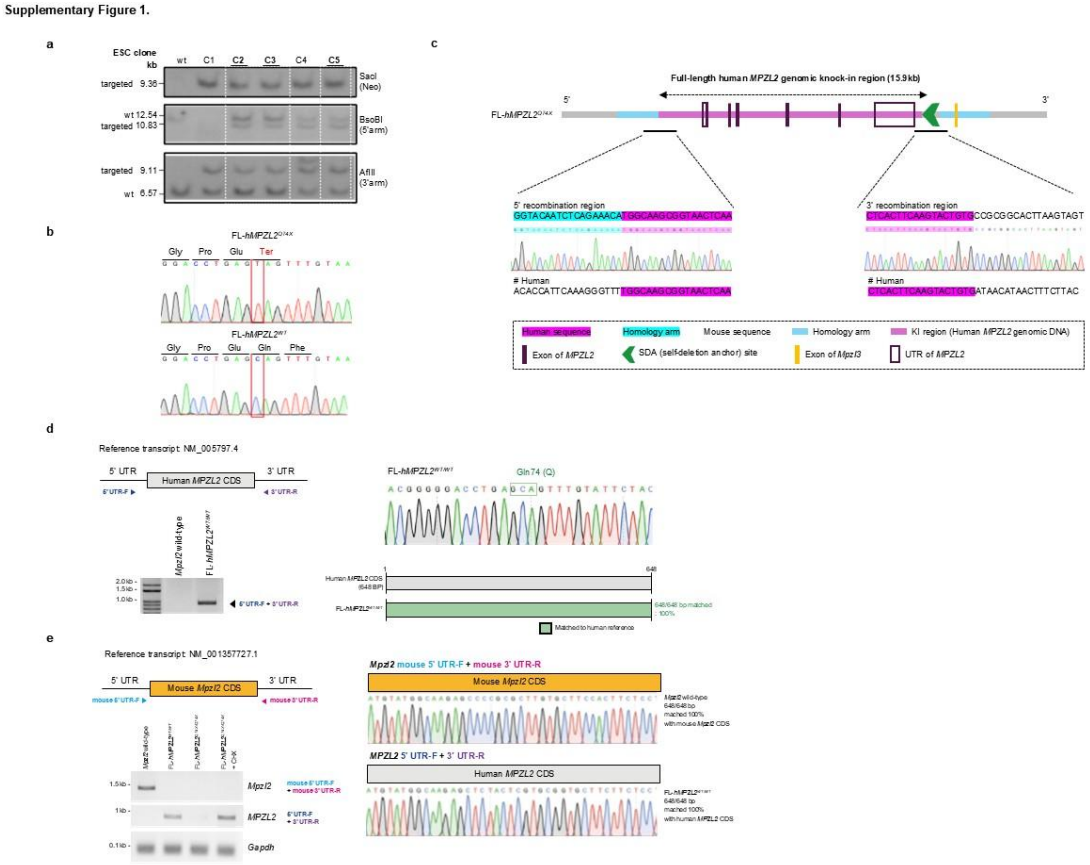

Figure S1. Genomic and transcript-level validation of the FL-*hMPZL2*$^{WT/WT}$ and FL-*hMPZL2*$^{Q74X/Q74X}$ mouse lines. (a) Southern blot analysis of targeted C57BL/6J ESCs using Neo-, 5′-arm-, and 3′-arm-specific probes. Three of five PCR-positive clones were confirmed to be correctly targeted. (b) Sanger sequencing confirming the c.220C>T variant in the FL-*hMPZL2*^{Q74X} allele and the corresponding reference sequence in the FL-*hMPZL2*^{WT} allele. (c) Targeting strategy for replacement of the endogenous mouse *Mpzl2* locus with the approximately 15.9-kb human *MPZL2* region. Sanger sequencing across the 5′ and 3′ recombination junctions confirmed the expected mouse–human boundary sequences. (d) RT–PCR spanning the full-length *MPZL2* coding sequence (CDS) and representative Sanger sequencing of the resulting cDNA from FL-*hMPZL2*$^{WT/WT}$ cochleae. Alignment with the human reference transcript (NM_005797.4) confirmed complete sequence identity and correct exon–exon splicing. (e) Species-specific RT-PCR analysis of in P56 cochleae using primer sets distinguishing mouse *Mpzl2* (NM_00357727.1) from human *MPZL2* (NM_005797.4). Endogenous mouse Mpzl2 was detected exclusively in wild-type mice, whereas human *MPZL2* was expressed in humanized lines, showing increased transcript accumulation in FL-h*MPZL2*$^{Q74X/Q74X}$ cochleae following cycloheximide (CHX) treatment. *Gapdh* served as an internal loading control. Representative sequencing verified the species-specific identities of the amplified mouse *Mpzl2* and human *MPZL2* products.

Supplementary Figure 2.

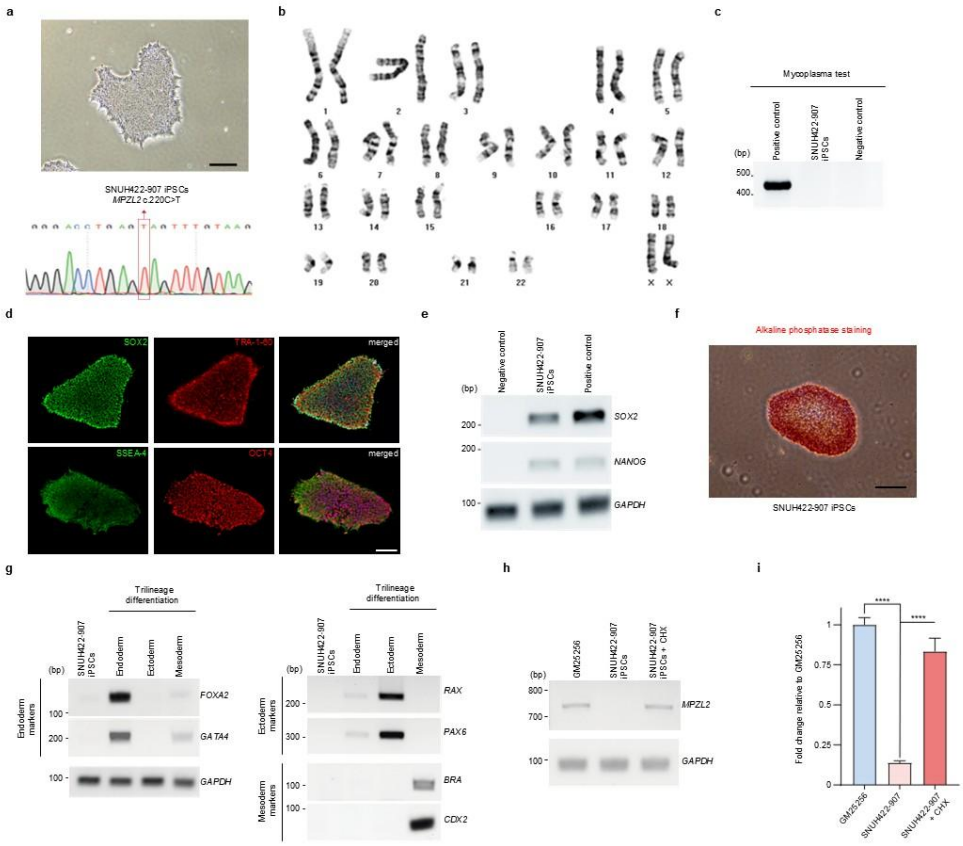

Figure S2. Characterization of patient-derived *MPZL2* c.220C>T iPSCs and validation of nonsense-mediated mRNA decay. (a) Representative phase-contrast image of patient-derived SNUH422-907 iPSCs homozygous for the *MPZL2* c.220C>T variant, with representative Sanger sequencing chromatogram confirming the homozygous c.220C>T substitution. Scale bar, 200 μm. (b) Representative karyotype of SNUH422-907 iPSCs showing a normal chromosomal complement. (c) PCR-based mycoplasma testing of SNUH422-907 iPSC cultures, with positive and negative controls. (d) Representative immunofluorescence images of SNUH422-907 iPSCs stained for the pluripotency markers SOX2, TRA-1-60, SSEA4 and OCT4. Scale bar, 100 μm. (e) RT–PCR analysis of the pluripotency markers *SOX2* and *NANOG* in SNUH422-907 iPSCs, with positive and negative controls. *GAPDH* served as an internal control. (f) Representative alkaline phosphatase staining of SNUH422-907 iPSC colonies. Scale bar, 200 μm. (g) RT–PCR analysis of trilineage differentiation of SNUH422-907 iPSCs. *FOXA2* and *GATA4* were used as endodermal markers, *RAX* and *PAX6* as ectodermal markers, and *BRA* and *CDX2* as mesodermal markers. *GAPDH* served as an internal control. (h) Representative RT–PCR analysis of *MPZL2* transcripts in GM25256 control iPSCs and SNUH422-907 iPSCs with or without cycloheximide (CHX) treatment. *GAPDH* served as an internal control. (i) qRT–PCR quantification of *MPZL2* transcript abundance in the groups shown in **h**. Expression levels were normalized to *GAPDH* and are presented relative to GM25256 control iPSCs. *MPZL2* transcript abundance in SNUH422-907 iPSCs was reduced to 13.91% ± 0.60% of the control level and increased to 83.32% ± 4.75% following CHX treatment, consistent with nonsense-mediated mRNA decay of the c.220C>T-containing transcript.

Supplementary Figure 3.

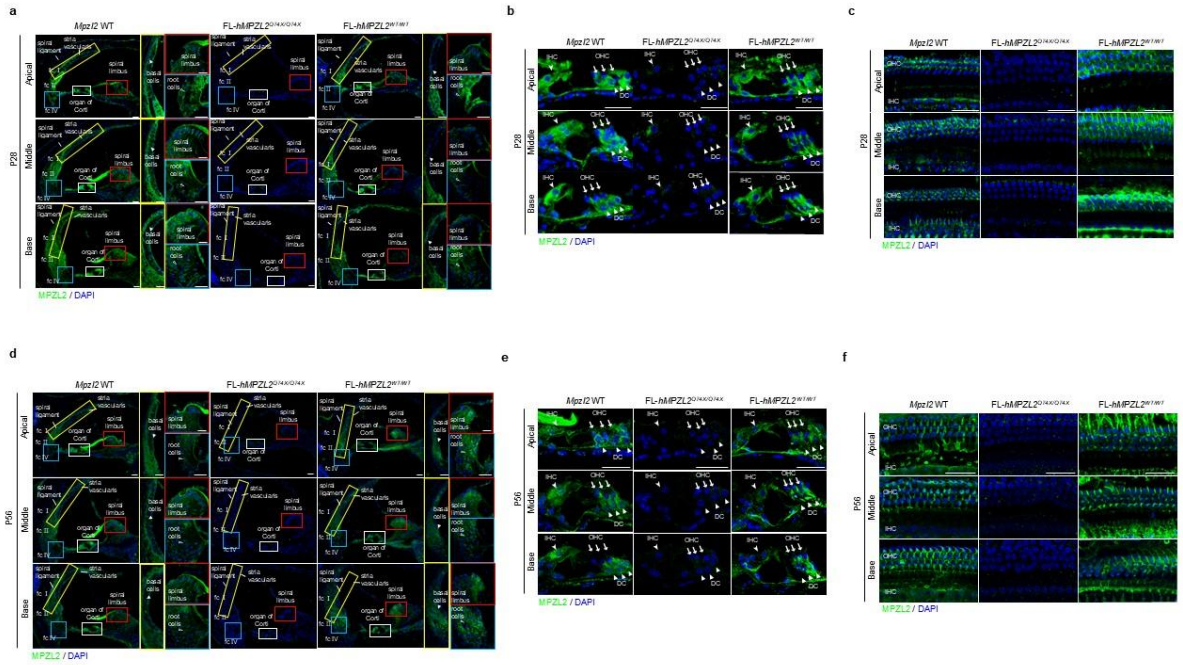

Figure S3. Spatiotemporal expression of MPZL2 in FL-*hMPZL2* humanized mice. (a, b) Representative low-magnification (×20; a) and (b) high-magnification (x80; b) mid-modiolar cryosections from *Mpzl2* WT, FL-*hMPZL2*$^{WT/WT}$, and FL-*hMPZL2*$^{Q74X/Q74X}$ mice at P28, immunolabeled for MPZL2 (green) and counterstained with DAPI (blue). Enlarged regions show MPZL2 expression in the organ of Corti (white rectangle), stria vascularis (yellow rectangle), spiral ligament, including type I, II, and IV fibrocytes (fc I, fc II, and fc IV), root cells (cyan rectangle), spiral limbus (red rectangle), and basal cells. (b) MPZL2 expression is shown in inner hair cells (IHCs), outer hair cells (OHCs), and Deiters' cells (DCs) across the apical, middle, and basal turns. (c) Representative whole-mount immunofluorescence (IF) images of the apical, middle, and basal turns at P28. (d-e) Representative low-magnification (×20; d) and high-magnification (x80; e) mid-modiolar cryosections from *Mpzl2* WT, FL-*hMPZL2*$^{WT/WT}$, and FL-*hMPZL2*$^{Q74X/Q74X}$ mice at P56. (f) Representative high-magnification whole-mount confocal images of the apical, middle, and basal turns at P56. In *Mpzl2* WT and FL-*hMPZL2*$^{WT/WT}$ mice, MPZL2 expression was examined in OHCs, and DCs, including the OHC–DC interface, including DC phalangeal processes (PhPs), and basolateral membranes and footplates of DC. Scale bars, 25 μm.

Supplementary Figure 4.

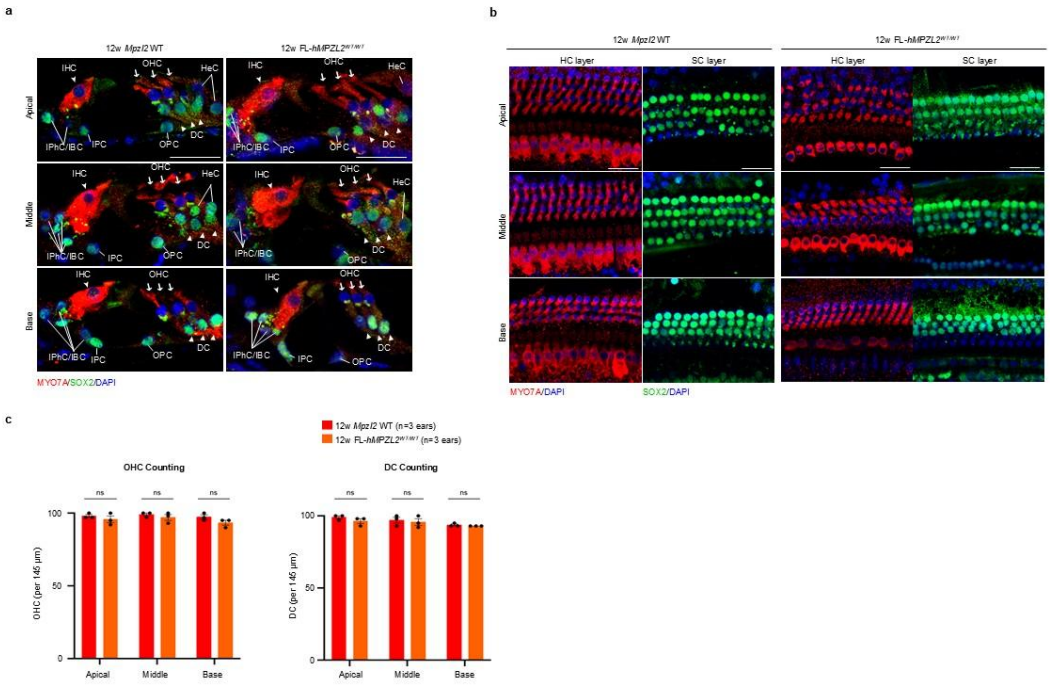

Figure S4. Histological assessment of FL-*hMPZL2*$^{WT/WT}$ mice. (a) Representative high-magnification (×80) cryosection IF images from the same groups (*n* = 3 ears per group; mean ± SEM). HCs were labeled with MYO7A (red), SCs, including DCs, with SOX2 (green), and nuclei with DAPI (blue). Scale bar, 25 μm**.** (b) Representative high-magnification (×80) whole-mount IF images of the apical, middle, and basal turns from 12-week-old *Mpzl2* WT and FL-*hMPZL2*$^{WT/WT}$ mice. Scale bar, 25 μm**.** (c) Quantification of OHC and DC counts in FL-*hMPZL2*$^{WT/WT}$ mice and *Mpzl2* WT mice (*n* = 3 ears per group; mean ± SEM). Statistical significance was determined by two-way ANOVA with Bonferroni's multiple-comparisons test. Each data point represents one ear obtained from a different mouse; thus, *n* denotes the number of mice.

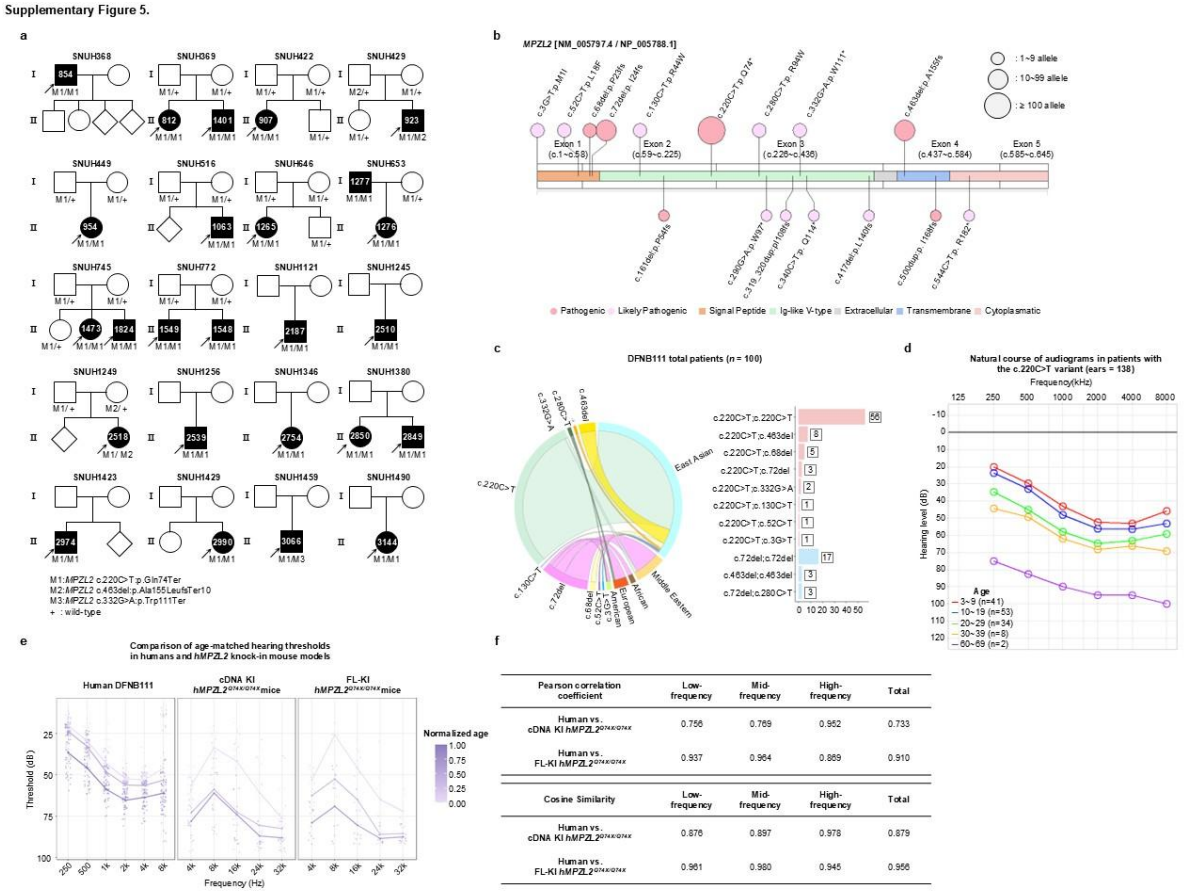

Figure S5. Natural history of *MPZL2* c.220C>T-associated DFNB111 and its recapitulation in full-length humanized *MPZL2* mice.

(a) In-house pedigrees and genotypes of 25 affected individuals from 20 unrelated families with *MPZL2*-associated DFNB111. Twenty-two individuals were homozygous for c.220C>T and three were compound heterozygous carrying c.220C>T *in trans* with a second pathogenic allele (M1/M2, n = 2; M1/M3, n = 1). M1, c.220C>T (p.Gln74Ter); M2, c.463del (p.Ala155LeufsTer10); M3, c.332G>A (p.Trp111Ter); +, wild-type allele. Squares, males; circles, females; diamonds, individuals whose sex is not disclosed; filled symbols, affected individuals; arrows, probands. (b) Lollipop plot of pathogenic/likely pathogenic *MPZL2* variants (NM_005797.4/NP_005788.1) compiled from our in-house cohort and ClinVar, mapped to exons and predicted protein domains. Circle size is proportional to the number of reported alleles (1–9, 10–99, ≥100) and circle color denotes ACMG/AMP classification for hearing loss. (c) Chord diagram showing the distribution of *MPZL2* alleles across genetic ancestry groups in 100 individuals with DFNB111 (in-house cohort together with ClinVar and published cases). The bar graph shows the observed biallelic genotype combinations and the number of individuals carrying each. c.220C>T was restricted to individuals of East Asian ancestry and was present in 74 of 100 individuals, of whom 56 were homozygous, identifying it as an East Asian founder allele. (d) Natural course of hearing loss in individuals carrying *MPZL2* c.220C>T, derived from 138 pure-tone audiograms (138 ears from 31 affected individuals) stratified by age at testing. Each line shows the mean air-conduction threshold for the indicated age group. (e) Comparison of the progressive hearing loss trajectory between

affected individuals (human; 250–8,000 Hz) and the cDNA knock-in (cDNA KI) and full-length knock-in (FL-KI) *hMPZL2*$^{Q74X/Q74X}$ mouse models (4–32 kHz). Thresholds are plotted against normalized age, indicated by color intensity (0, youngest; 1, oldest); human age ranges of 3–9, 10–19 and 20–39 years were matched to 4, 8 and 12 weeks of age in mice. (f). Pearson correlation coefficients and cosine similarities between the human and mouse normalized audiometric trajectories, calculated separately for low, mid and high frequencies and across all tested frequencies (total). Low frequency, 250 and 500 Hz (human) and 4 and 8 kHz (mouse); mid frequency, 1 and 2 kHz (human) and 16 kHz (mouse); high frequency, 4 and 8 kHz (human) and 24 and 32 kHz (mouse).

Supplementary Figure 6.

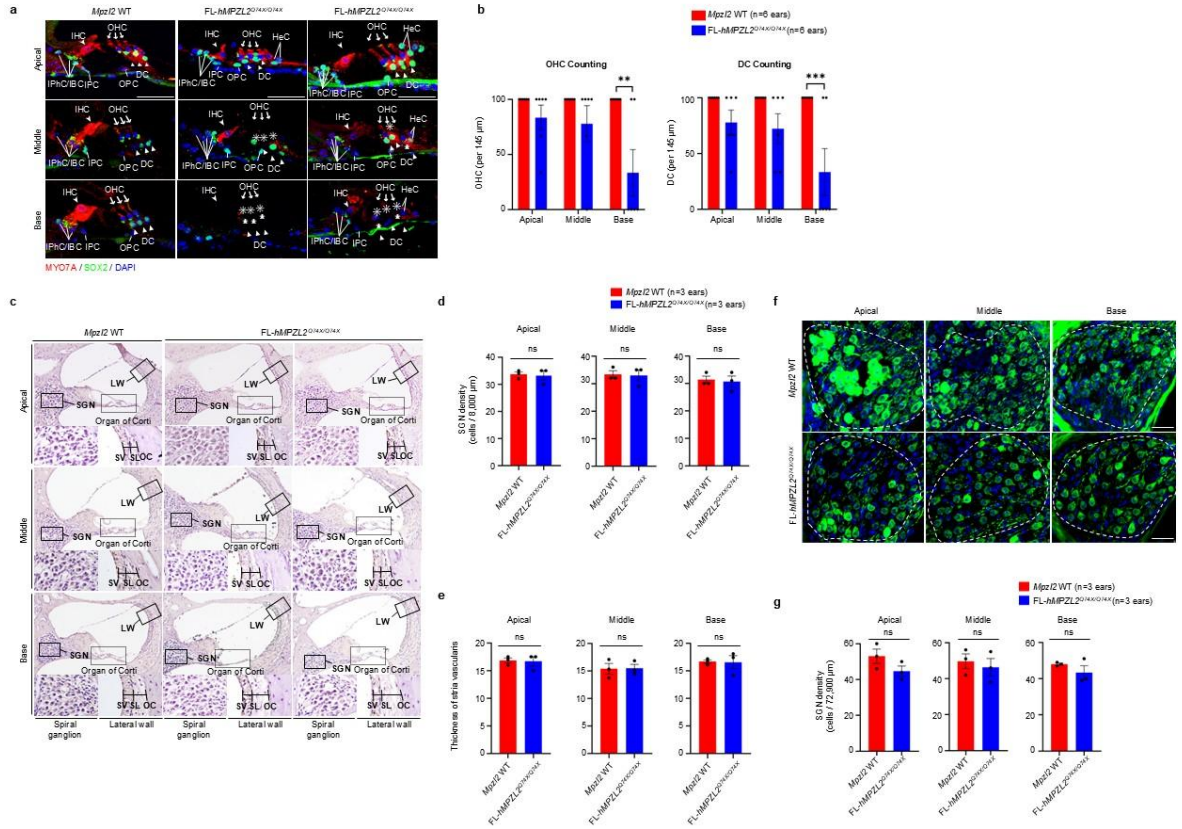

Figure S6. Histological assessment of the cochlear structure in FL-*hMPZL2*$^{Q74X/Q74X}$ mice. (a) Representative high-magnification mid-modiolar cryosection IF images of the apical, middle, and basal turns from *Mpzl2* WT and FL-*hMPZL2*$^{Q74X/Q74X}$ mice at 12 weeks of age. HCs and SCs were labeled with MYO7A (red) and SOX2 (green), respectively. Arrowheads indicate IHCs and DCs, white arrows point to OHCs, and white lines mark SCs. Asterisks indicate loss of OHCs and DCs. Scale bars, 25 μm. (b) Quantification of OHC and DC numbers per 145 μm in the apical, middle, and basal turns of *Mpzl2* WT and FL-*hMPZL2*$^{Q74X/Q74X}$ mice (n = 6 ears per group; mean ± SEM). Statistical analysis was performed using two-way ANOVA with Bonferroni's multiple-comparisons test. (c) Representative hematoxylin and eosin (H&E)-stained mid-modiolar cochlear sections from *Mpzl2* WT and FL-*hMPZL2*$^{Q74X/Q74X}$ mice at 12 weeks of age. Boxed regions indicate the SGN, lateral wall (LW), and organ of Corti; corresponding enlarged views show the SGN, stria vascularis (SV), spiral ligament (SL), and organ of Corti. (d) Quantification of SGN density in H&E-stained sections from the apical, middle, and basal turns (cells per 8,000 μm²) (n = 6 ears per group; mean ± SEM). (e) Quantification of stria vascularis thickness in the apical, middle, and basal turns (n = 3 ears per group; mean ± SEM). Statistical significance was determined using two-way ANOVA with Bonferroni's multiple-comparisons test. ns, not significant. (f) Representative high-magnification cryosection IF images of TUBB3-positive SGNs (green) in the apical, middle, and basal turns; nuclei were counterstained with DAPI (blue). (g) Quantification of TUBB3-positive SGN density in cryosections from the apical, middle, and basal turns

(cells per 72,900 μm²) (*n* = 3 ears per group; mean ± SEM). Statistical significance was determined using Kruskal-Wallis with Dunn's multiple-comparisons test. ns, not significant. Individual points represent different mouse ears.

Supplementary Figure 7.

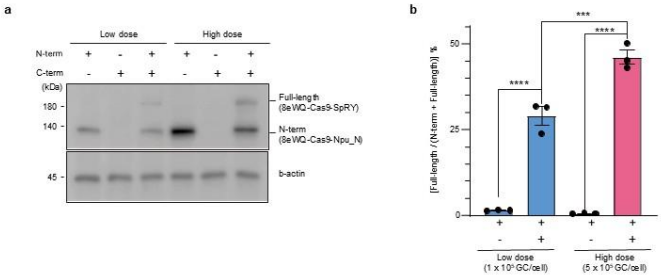

Figure S7. Dose-dependent split-intein reconstitution of full-length ABE8eWQ–SpRY. (a) Representative western blot showing the reconstitution of full-length ABE8eWQ–SpRY following co-transduction with the N- and C-terminal viruses under low-dose (1×10^5 genome copies per cell) and high-dose (5×10^5 genome copies per cell) conditions. Cells transduced with the N- or C-terminal virus alone served as controls. The full-length reconstituted editor and the N-terminal fragment were detected using an antibody against the N-terminal Cas9 region; β-actin served as a loading control. (b) Quantification of editor reconstitution, calculated as the abundance of full-length ABE8eWQ–SpRY relative to the combined abundance of the N-terminal fragment and the full-length editor. Reconstitution efficiency increased from 29.05% ± 4.05% under the low-dose condition to 46.02% ± 3.65% under the high-dose condition. Data are presented as mean ± SEM (n = 3 independent experiments).

Supplementary Figure 8.

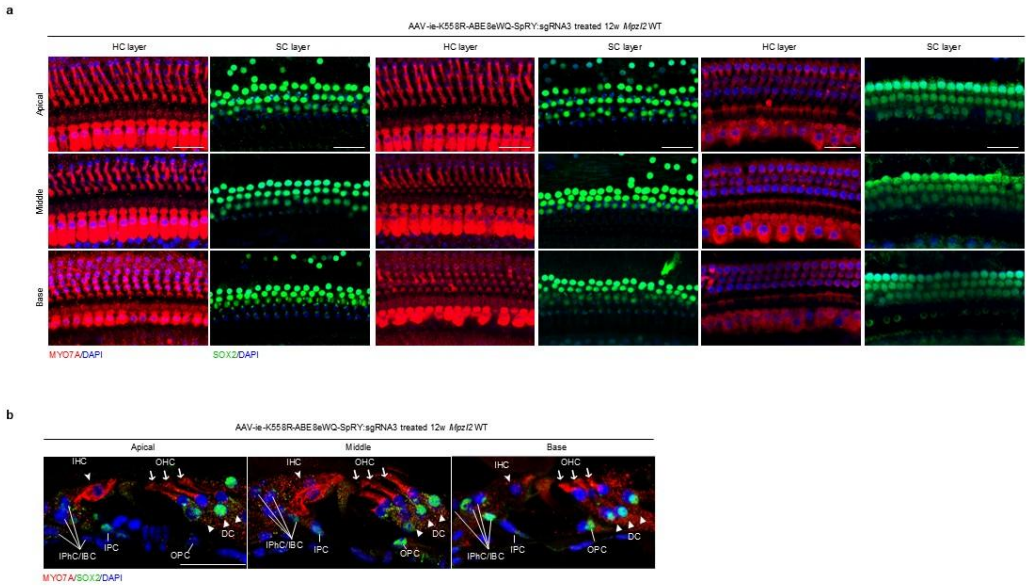

Figure S8. Organ of Corti morphology following high-titer AAV-ie-K558R-ABE8eWQ–SpRY:sgRNA3 administration. (a) Representative high-magnification (×80) whole-mount IF images of the apical, middle, and basal turns from *Mpzl2* WT mice treated at P14–P15 and harvested at 12 weeks of age. HC and SC layers are shown separately. HCs were labeled with MYO7A (red), SCs, with SOX2 (green), and nuclei with DAPI (blue). (b) Representative high-magnification (×80) mid-modiolar cryosection IF images of the organ of Corti from treated *Mpzl2* WT mice at 12 weeks of age. Arrowheads indicate IHCs and DCs, and white arrows indicate OHCs. White lines mark SCs, including inner phalangeal cell/inner border cell (IPhC/IBC), inner pillar cell (IPC), outer pillar cell (OPC). Scale bar, 25 μm.

Supplementary Figure 9.

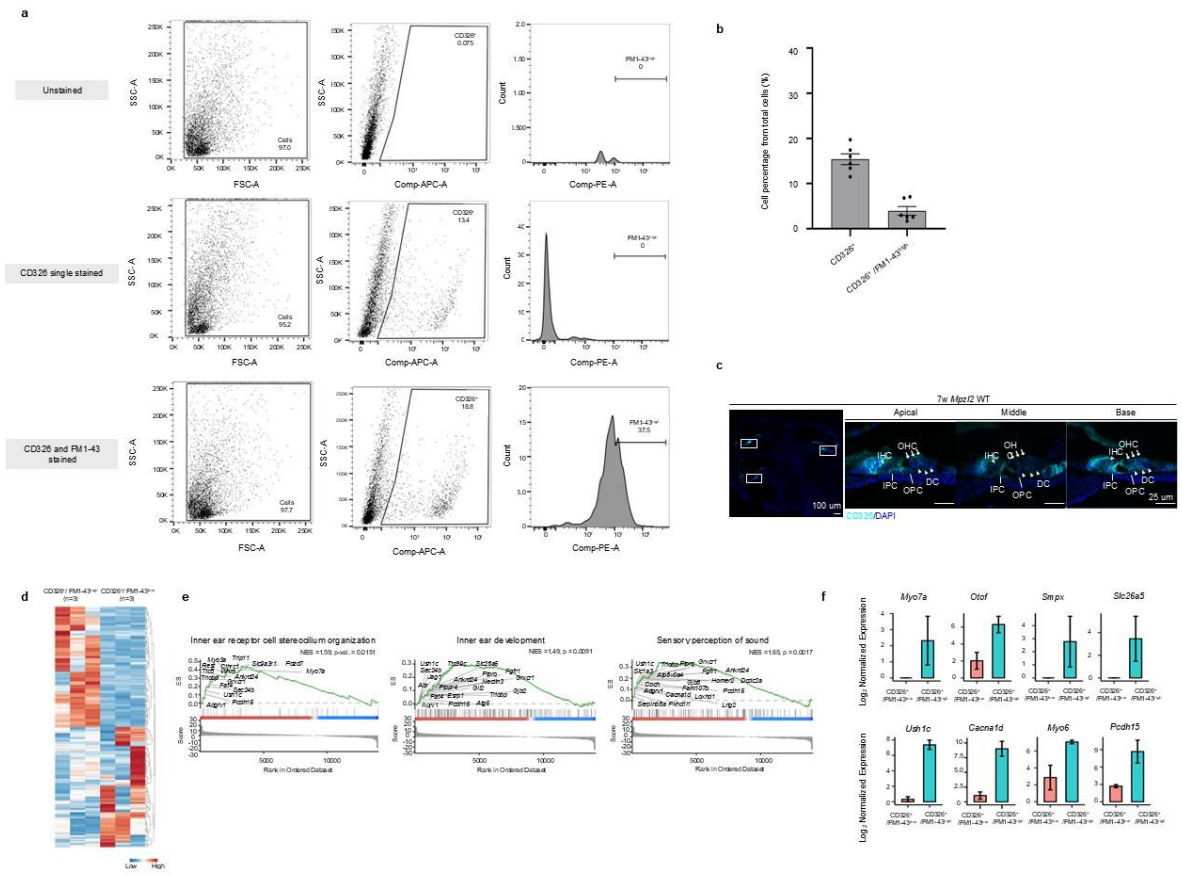

Figure S9. FACS gating strategy of CD326⁺ and CD326⁺/FM1-43^{high} cells and molecular characterization of organ of Corti epithelial cells. (a) Representative flow-cytometry gating strategy for dissociated organ of Corti cells. Cells were first gated according to forward- and side-scatter properties. CD326⁺ cells were subsequently identified by APC fluorescence, and the FM1-43^{high} population was gated within the CD326⁺ population. (b) Percentages of CD326⁺ and CD326⁺/FM1-43^{high} cells among the total gated cell population. Each dot represents an individual cochlear sample, and bars show the mean ± SEM (*n* = 6 ears). (c) Representative IF staining images of a whole cochlear section (magnification x10) (left) and organ of Corti from apical, middle and basal turns (magnification x40) (right) showing CD326 (cyan) expression within the sensory epithelium in 7-week *Mpzl2* WT. Images are representative of *n* = 3 ears. Scale bar, 100um and 25um, respectively. (d) Illumina-based bulk RNA sequencing was performed on CD326⁺/ FM1-43^{high} and CD326⁺/ FM1-43^{low} cells isolated by fluorescence-activated cell sorting (FACS) from single-cell suspensions of the organ of Corti of FL-*hMPZL2*$^{WT/WT}$ mice. Three independently prepared samples were analyzed per fraction; each sample comprised of cochlea from *n* = 6 ears. Heatmap analysis of upregulated (red) and downregulated (blue) genes from bulk RNA-seq characterization of CD326⁺/FM1-43^{high}, and CD326⁺/FM1-43^{low} cell fractions. (e) Gene set enrichment analysis (GSEA) plots were significant for inner ear receptor cell stereocilium organization (GO:0060122), inner ear development (GO:0048839), and sensory perception of sound pathways (GO:0007605). GSEA was performed using the full ranked gene list according to the DESeq2 Log_2fold change values to evaluate pathway-level enrichment between CD326⁺/FM1-43^{high} and

CD326^{+}/FM1-43^{low} groups. The top 20 leading edge genes were labeled. (f) Bar plot of Log_2 normalized expression of cochlear hair cell-associated *genes Myo7a, Otof, Smpx, Slc26a5, Ush1c, Cacna1d, Myo6, and Pcdh15*. n = 3 replicates per group; mean ± SEM.

Supplementary Figure 10.

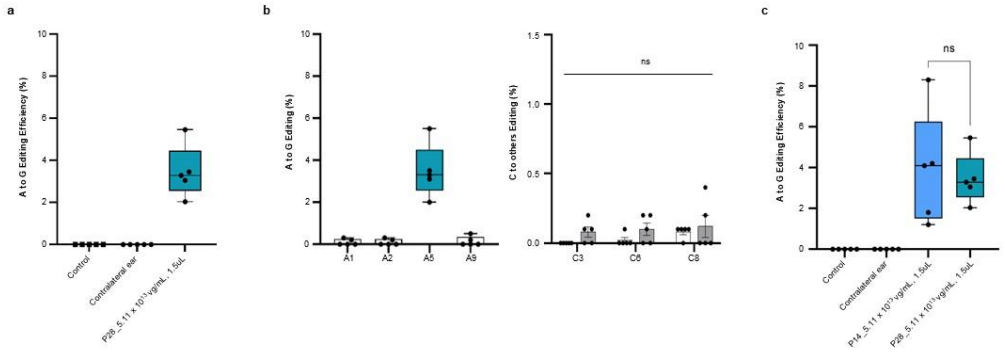

Figure S10. On-target and bystander editing in the organ of Corti following post maturation treatment. (a) Targeted deep-sequencing analysis of A-to-G editing at the target A5 position in organ of Corti samples from uninjected control ears, contralateral ears, and injected ears of FL-*hMPZL2*$^{Q74X/Q74X}$ mice treated at P28 with AAV-ie-K558R-ABE8eWQ–SpRY:sgRNA3 (1.5 µL per ear; 5.11 × 10^{13} vg/mL; *n* = 5 ears per group; mean ± SEM). (b) A-to-G editing frequencies at adenine positions within the editing window (left) and non-canonical cytosine editing frequencies at C3, C6, and C8 (right) in injected organ of Corti samples (*n* = 5 ears per group; mean ± SEM). (c) Comparison of A5 editing efficiencies in organ of Corti samples after treatment at P14 or P28. Individual points represent ears (*n* = 5 ears per group; mean ± SEM). Each data point represents one ear obtained from a different mouse; thus, *n* denotes the number of mice. Statistical analysis was performed using one-way ANOVA with Bonferroni's multiple-comparisons test. ns, not significant.

Supplementary Figure 11.

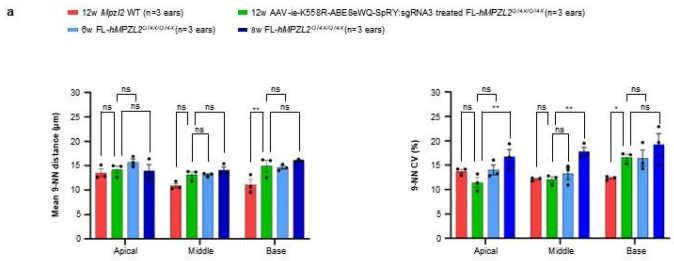

Figure S11. 3D quantification of DC disorganization after post-maturation treatment. (a) Mean 9-NN distance (left) and 9-NN CV (right) of SOX2-positive DC nuclei in the apical, middle, and basal cochlear turns of 12-week-old *Mpzl2* WT mice (red) and P28–P30-treated FL-*hMPZL2*$^{Q74X/Q74X}$ mice (green), and untreated FL-*hMPZL2*$^{Q74X/Q74X}$ mice analyzed at 6 weeks (light blue) or 8 weeks (dark blue). Between the 12-week-old WT and treated groups, both metrics were comparable between groups in the apical and middle turns but remained significantly elevated in the basal turn of treated mice, indicating residual basal-turn DC disorganization. Each data point represents one ear obtained from a different mouse. Data are presented as mean ± SEM (n = 3 ears per group). Statistical significance was determined using two-way ANOVA with Bonferroni's multiple-comparisons test. ns, not significant; *P < 0.05; **P < 0.01.

Supplementary Figure 12.

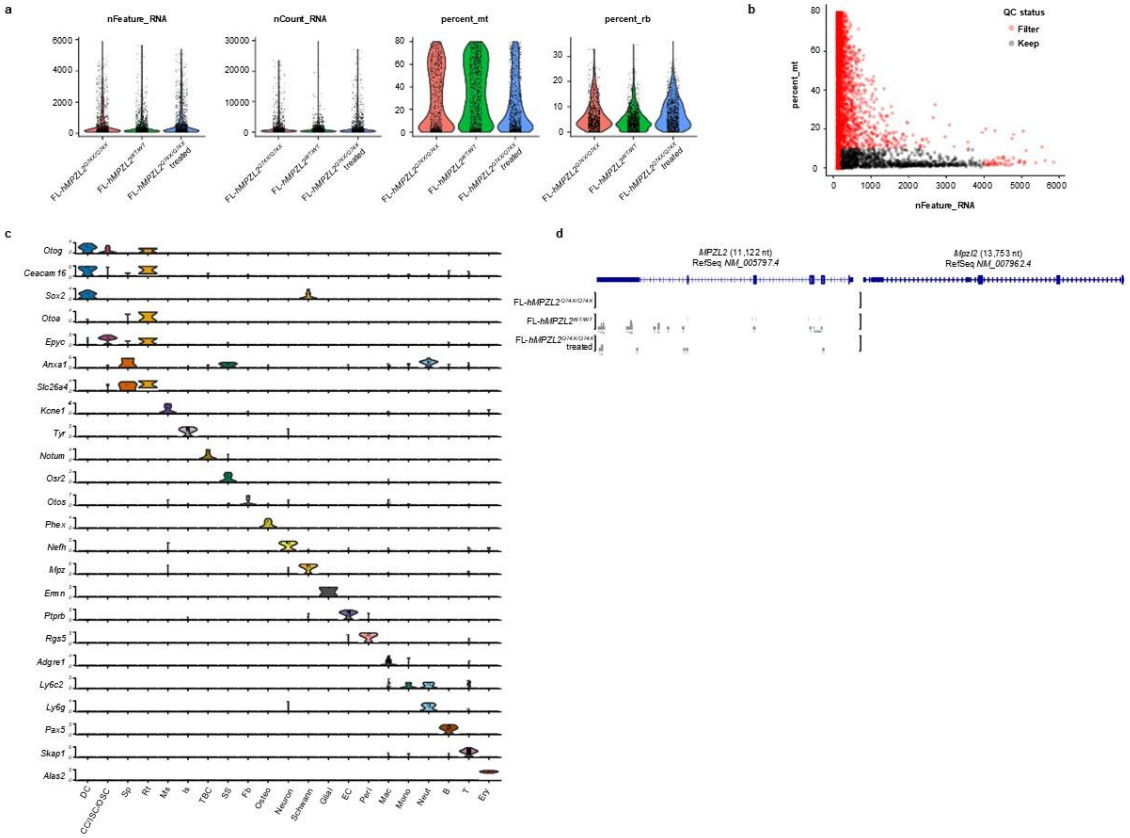

Figure S12. Quality control, cell-type annotation, and locus-specific transcript mapping of cochlear scRNA-seq datasets. (a) Quality-control metrics for FL-*hMPZL2*$^{Q74X/Q74X}$, FL-*hMPZL2*$^{WT/WT}$ and treated FL-*hMPZL2*$^{Q74X/Q74X}$ scRNA-seq datasets. Violin plots show the number of detected genes per cell (nFeature_RNA), total unique molecular identifier counts per cell (nCount_RNA), percentage of mitochondrial transcripts (percent_mt), and percentage of ribosome-associated transcripts (percent_rb). Scatterplots show percent_mt relative to nFeature_RNA. Cells retained after quality-control filtering are shown in gray, and excluded cells are shown in red. (b) Violin plots showing the normalized expression of representative marker genes used to annotate 21 cochlear cell populations. Abbreviations: Deiter's cells (DC), Claudius cells (CC), Inner–outer sulcus cells (ISC-OSC), Marginal cells (MS), Intermediate stria cells(IS), Spindle cells (Spindle), Root cells (Root), Fibrocytes (Fb), Macrophages (Mac), Mono (Monocytes), Neutrophils (Neut), Tympanic border Cells (TBC), Osteocytes (Osteo), Surrounding structure Cells (SD), Endothelial Cells(EC), Pericytes (Peri), Schwann Cells (Sch). (c) Genomic organization and representative scRNA-seq read-alignment tracks for the human *MPZL2* and mouse *Mpzl2* loci. Blue gene models show the exon–intron structures of human *MPZL2* (11,122 nt; RefSeq NM_005797.4) and mouse *Mpzl2* (13,753 nt; RefSeq NM_007962.4). Reads aligned to the human *MPZL2* locus in FL-*hMPZL2*$^{WT/WT}$, and treated FL-*hMPZL2*$^{Q74X/Q74X}$ whereas no corresponding reads were detected in FL-*hMPZL2*$^{Q74X/Q74X}$. No reads aligning to the endogenous mouse *Mpzl2* locus were detected in all conditions.

Supplementary Figure 13.

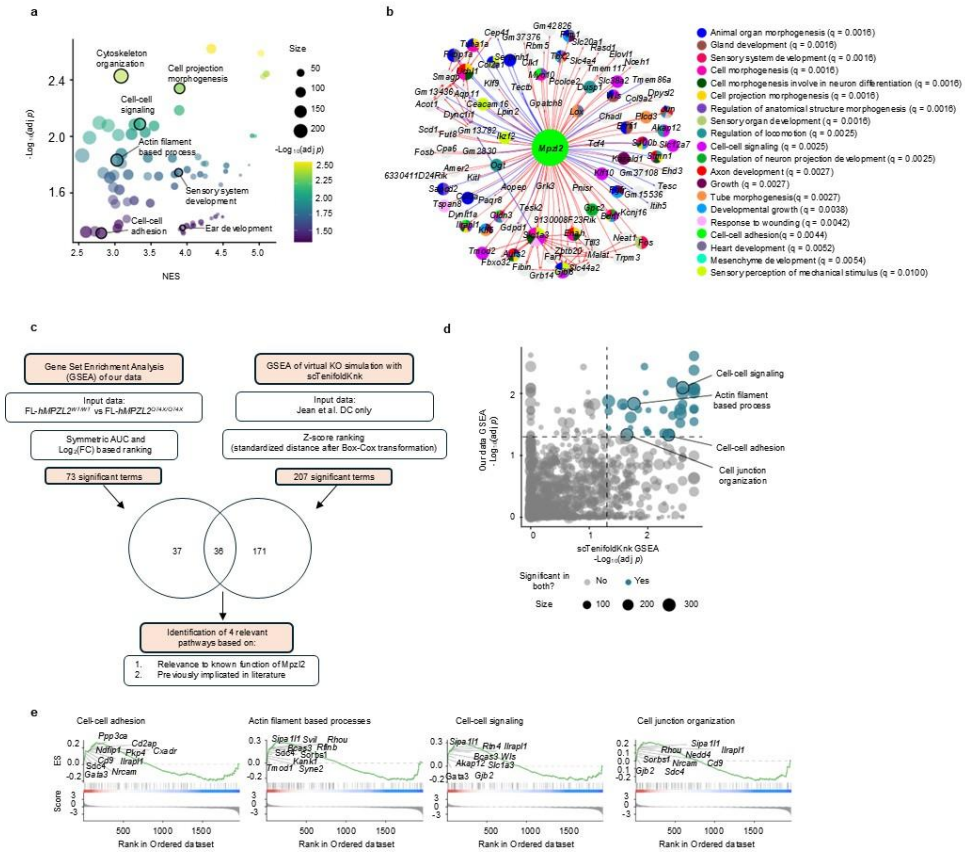

Figure S13. Convergent transcriptomic analyses identify adhesion- and cell structure-related pathways associated with *Mpzl2* deficiency. (a) GSEA with transcriptional differences between FL-*hMPZL2*$^{WT/WT}$ and FL-*hMPZL2*$^{Q74X/Q74X}$ in DCs. Significantly enriched Gene Ontology biological process (GO:BP) terms are plotted according to their NES and -Log$_{10}$(adj *P* value). Circle size represents gene-set size, and color indicates statistical significance. Selected terms related to Mpzl2 function and inner ear function are labeled. (b) Egocentric plot of *Mpzl2*-centered gene regulatory network generated using scTenifoldKnk. GSEA of the predicted transcriptional perturbation and representative significantly enriched GO:BP terms are indicated by the color key, with the corresponding false-discovery rate (*q* value) shown. (c) Workflow used to identify pathways shared between the experimental and in silico perturbation analyses. Experimental GSEA was performed using genes ranked by symmetric area under the receiver operating characteristic curve (AUC) and Log$_2$(FC), identifying 73 significant terms. For the scTenifoldKnk analysis, DCs from the reference dataset were subjected to virtual *Mpzl2* knockout, and genes were ranked using Z-scores derived from standardized perturbation distances following Box–Cox transformation, identifying 207 significant terms. Comparison of the two analyses identified 36 overlapping terms; 37 and 171 terms were unique to the experimental and scTenifoldKnk analyses, respectively. Overlapping terms were subsequently prioritized based on previously reported *Mpzl2* associated functions and their relevance to the observed cellular phenotype. (d) Comparison of adjusted *P* values obtained from the experimental and scTenifoldKnk-based GSEA results. Each circle represents a GO:BP term, and circle size represents gene-set size. Teal circles indicate pathways significant in both analyses. Dashed lines indicate the adjusted *P* = 0.05 threshold. Selected overlapping

pathways are labeled. (e) GSEA running enrichment-score plots for four prioritized overlapping GO:BP terms: cell–cell adhesion, actin filament-based processes, cell–cell signaling, and cell junction organization. Labeled genes indicate representative leading-edge contributors to each enrichment signal.

Supplementary Figure 14.

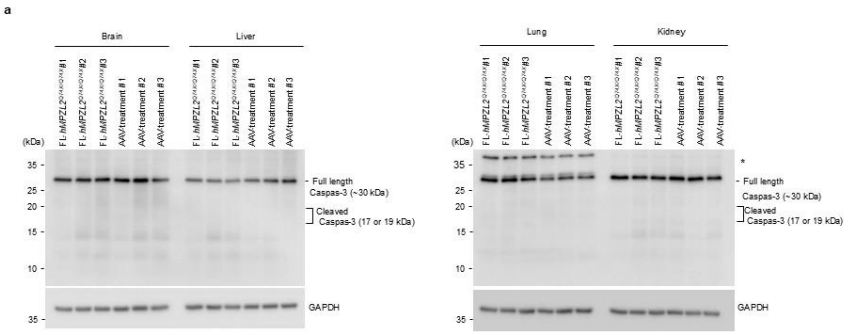

Figure S14. Assessment of apoptosis in peripheral organs following inner ear administration of the dual-AAV base-editing system. Representative immunoblot analysis of full-length and cleaved caspase-3 in the brain, liver, lung and kidney of untreated and dual-AAV-treated FL-*hMPZL2*$^{Q74X/Q74X}$ mice. Tissues were collected at P28–P30 following PSCC administration at P14–P15. Full-length caspase-3 (~30 kDa) and cleaved caspase-3 (17 or 19 kDa) are indicated; GAPDH served as a loading control (n = 3 mice per group). Asterisk indicates a non-specific band.

Supplementary Figure 15.

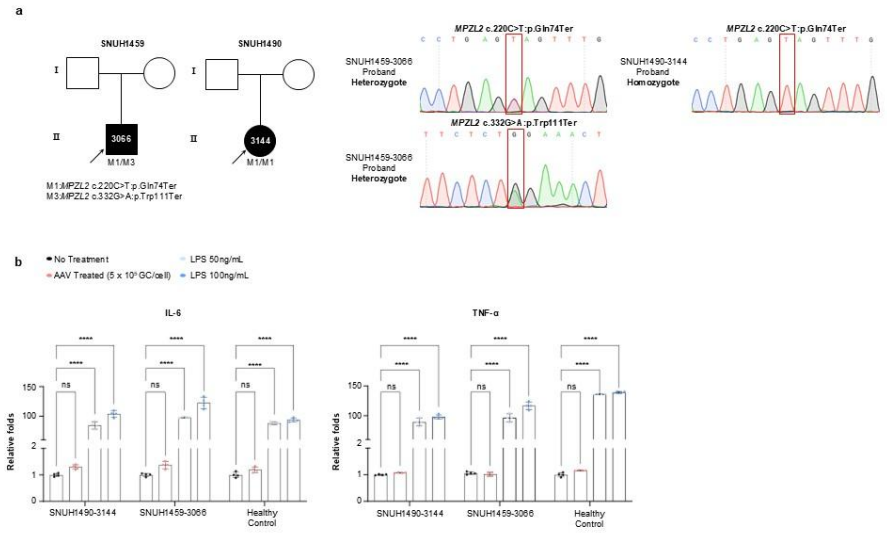

Figure S15. Inflammatory response to the dual-AAV base-editing system in human PBMCs. (a) Pedigrees of the SNUH1459 and SNUH1490 families. PBMC donors SNUH1459-3066 and SNUH1490-3144, both carrying the MPZL2 c.220C>T variant, are indicated by arrows; filled symbols denote affected individuals. (b) IL-6 and TNF-α secretion from PBMCs obtained from SNUH1459-3066, SNUH1490-3144 and a healthy donor following 24-h exposure to the dual-AAV base-editing system at 5×10^5 genome copies per cell. Untreated cells served as negative controls, and lipopolysaccharide (LPS) at 50 or 100 ng/mL served as a positive controls. Cytokine concentrations were measured by ELISA and normalized to the corresponding untreated controls. Data are presented as mean ± SEM (n = 3 independent experiments). Statistical significance was determined using two-way ANOVA with Bonferroni's multiple-comparison test; ns, not significant; ns, not significant; ****$P < 0.0001$